

## Supporting Information

### Electronically transparent Au-N bonds for molecular junctions

Yaping Zang,<sup>1,§</sup> Andrew Pinkard,<sup>2,§</sup> Zhen-Fei Liu,<sup>3</sup> Jeffrey B. Neaton,<sup>3</sup> Michael L. Steigerwald,<sup>2</sup> Xavier Roy,<sup>2\*</sup> Latha Venkataraman<sup>1,2\*</sup>

1. Department of Applied Physics, Columbia University, New York, New York 10027, USA
2. Department of Chemistry, Columbia University, New York, New York 10027, USA
3. Molecular Foundry, Lawrence Berkeley National Laboratory, Department of Physics, University of California, Berkeley, California 94720, USA

\* e-mail: (L.V.) lv2117@columbia.edu; (X.R.) xr2114@columbia.edu

§Contributed equally to this work.

#### Table of Contents:

1. General Experimental Details.
2. Synthetic Details.
3. STM-BJ Methods
4. DFT based Transmission Calculations
5. Additional Data
6. Mass-Spectroscopy Data
7. References

## 1. General Experimental Details.

Mass spectra were obtained at the Columbia University mass spectrometry facility using a XEVO G2-XS Waters® equipped with a QTOF detector with multiple inlet and ionization capabilities including electrospray ionization (ESI), atmospheric pressure chemical ionization (APCI), and atmospheric solids analysis probe (ASAP). The base peaks were usually obtained as [M]<sup>+</sup> or [M+H]<sup>+</sup> ions.

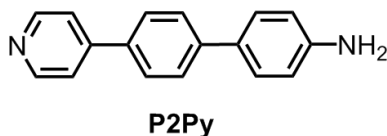
## 2. Synthetic Details.

Unless otherwise stated, chemicals were used as received from their respective commercial sources. 4,4'-dibromobiphenyl was purchased from Acros Organics. All other chemicals, including **P2** and **P3**, were purchased from Sigma Aldrich. Dry and deoxygenated solvents were prepared by elution through a dual-column solvent system (MBraun SPS). Compound **P4**<sup>1</sup> and starting material 4,4'-dibromoquarterphenyl<sup>2</sup> were prepared according to published literature procedures. Intermediate *tert*-butyl(4'-bromo-[1,1'-biphenyl]-4-yl)carbamate<sup>3</sup> was adapted from a published literature procedure and is reported below. **P5** and **P6** were prepared in a similar fashion to **P4**, except that 4,4'-dibromoterphenyl and 4,4'-dibromoquarterphenyl were used instead of 4,4'-dibromobiphenyl. An example synthesis is given below.

Synthesis of **P5**: 4,4'-Dibromoterphenyl (0.500 g, 1.29 mmol), 4-(N-Boc-amino)phenylboronic acid pinacol ester (0.864 g, 2.71 mmol), cesium fluoride (0.783 g, 5.15 mmol), tetrakis(triphenylphosphine)palladium(0) (0.075 g, 5 mol %) were combined in a pressure vessel with a teflon screw-cap and gently purged with nitrogen. Anhydrous THF (40 mL) was added, the vessel was sealed and stirred at 80 °C for 16 h. The mixture was cooled to room temperature and the resulting solid was collected by filtration. The solid was washed with water, followed by THF. The solid was then suspended in dichloromethane and cooled to 0 °C to which 12 mL of trifluoroacetic acid was added. The reaction was warmed to room temperature and stirred for 16 h. The reaction was filtered and basified by the addition of 3.2 g of NaOH in 100 mL of water. The resulting solid was washed with dichloromethane, water, and acetone to give the desired product as an off-white solid (0.070 g, 13% yield).

<sup>1</sup>H NMR (300 MHz, DMSO-d<sub>6</sub>, 25 °C) δ = 4.00 (br), 6.85 (s, 4 H), 7.68 (m, 16 H). HRMS calculated for C<sub>30</sub>H<sub>25</sub>N<sub>2</sub><sup>+</sup> [M+H]<sup>+</sup> 413.2018, observed 413.2016 [M+H]<sup>+</sup>.

Synthesis of **P6**: The compound was synthesized using the same method as above, except using 4,4'-dibromoquarterphenyl. The desired product was obtained as a tan solid (0.095g, 20% yield). Insolubility of the compound precluded <sup>1</sup>H NMR characterization. HRMS calculated for C<sub>36</sub>H<sub>28</sub>N<sub>2</sub><sup>+</sup> [M+H]<sup>+</sup> 489.2331, observed 489.2332 [M+H]<sup>+</sup>.



### Synthesis of P2Py:

**P2Py** was synthesized by first preparing *tert*-butyl(4'-bromo-[1,1'-biphenyl]-4-yl)carbamate from an adapted literature procedure.<sup>3</sup> 1,4-dibromobenzene (3.70 g, 3.68 mmol), 4-(N-Boc-amino)phenylboronic acid pinacol ester (1.00 g, 3.14 mmol), cesium carbonate (2.04 g, 6.26 mmol), and tetrakis(triphenylphosphine)palladium(0) (0.362 g, 10 mol %) were combined in Schlenk flask and placed under nitrogen. Toluene (20 mL) and Argon-sparged deionized water (40 mL) were added to the mixture. The reaction was refluxed for 72 h and then cooled to room temperature. The phases were separated in a separatory funnel and the organic layer was extracted with ethyl acetate, dried with MgSO<sub>4</sub> and concentrated. The residue was purified by silica gel chromatography (gradient of 0 to 70 % dichloromethane in hexanes). The solvents were removed *in vacuo* to give the desired product, *tert*-butyl(4'-bromo-[1,1'-biphenyl]-4-yl)carbamate, as a white, fluffy solid (0.864 g, 80% yield). <sup>1</sup>H NMR (300 MHz, DMSO-d<sub>6</sub>, 25 °C) δ = 1.48 (s, 9 H), 7.62 (m, 12 H), 9.43 (s, 1 H).

*tert*-Butyl(4'-bromo-[1,1'-biphenyl]-4-yl)carbamate (0.475 g, 1.36 mmol), 4-(Boc-amino)pyridine (0.308 g, 1.59 mmol), cesium fluoride (0.414 g, 2.73 mmol), and tetrakis(triphenylphosphine)palladium(0) (0.089 g, 5 mol %) were combined in a Schlenk flask and purged with nitrogen. The flask was sealed under nitrogen and 100 mL of anhydrous THF was added. The reaction was refluxed for 16 h, and then cooled to room temperature. The solvent was removed *in vacuo* and the resulting solid was washed with water and dichloromethane and suspended in dichloromethane. The mixture was cooled to 0 °C to which 12 mL of trifluoroacetic was added. The reaction was stirred for 16 h and basified by the addition of 2.0 M NaOH. The product was filtered and washed with dichloromethane, followed by water and dried under high vacuum to give an off-white solid (0.086 g, 26% yield). <sup>1</sup>H NMR (300 MHz, DMSO-d<sub>6</sub>, 25 °C) δ = 5.26 (s, 2 H), 6.66 (m, 2 H), 7.51 (m, 2 H), 7.70 (m, 4 H), 7.81 (m, 2 H), 8.61 (m, 2 H). HRMS calculated for C<sub>17</sub>H<sub>14</sub>N<sub>2</sub><sup>+</sup> [M+H]<sup>+</sup> 247.1238, observed 247.1235 [M+H]<sup>+</sup>.

### **3. STM-BJ Method.**

Conductance measurements: Conductance measurements were carried out using a custom-built scanning tunneling microscope that has been previously described in detail.<sup>4</sup> Conductance measurements were carried out in dilute solutions (10 μM) in propylene carbonate with tetrabutylammonium perchlorate as a supporting electrolyte unless otherwise specified. The insulated tips were created by driving a mechanically cut gold tip through Apiezon wax.<sup>5</sup> One-dimensional conductance histograms are constructed using

logarithmic bins (100/decade), and two-dimensional histograms use logarithmic bins along the conductance axis (100/decade) and linear bins along the displacement axis. All histograms are constructed without any data selection.

Current-Voltage Measurements: I-V measurements were performed using the STM-BJ, with a slightly modified procedure. Instead of continuously retracting the tip from the substrate, the tip was withdrawn for 150 ms, held for 150 ms and then withdrawn for an additional 200 ms to fully rupture the molecular junction. A constant voltage was applied during the initial and final segments, as well as during the first and last 25 ms when the tip position is held fixed. During the central 100 ms while the tip was held, a voltage sweeps first going up to +0.9 V, then down to -0.9 V and finally back to 0 V was applied. Current was measured during the entire 500 ms procedure. I-V data was analyzed by first selecting traces with a molecular junction during the first 25 ms period when the tip was held fixed. Traces were selected by using an automated algorithm that required the conductance during the positive ramp to be within or higher than the conductance peak at low bias. Most I-V traces did not sustain the negative -0.9 V applied. After trace selection, all I-Vs were used to construct a two-dimensional current versus time/voltage histogram shown in the manuscript.

#### **4. DFT based Transmission Calculations.**

We relax the junction geometries with density functional theory (DFT) using the Perdew-Burke-Ernzerhof (PBE) functional<sup>6</sup> as implemented in SIESTA<sup>7</sup> package. Pseudopotentials and basis sets are adapted from a previous work<sup>8</sup>: a single-zeta polarization basis set is used for Au atoms and double-zeta polarization basis sets are used for other elements. Norm-conserving pseudopotentials are used, and for Au, the pseudopotential and basis set are tuned to match the experimental work function of Au(111) surface. Seven junctions are relaxed: **P2–P4** with (a) one new Au–N and one dative Au←N contact; and (b) two dative Au←N contacts, respectively, as well as **P4** with two new Au–N contacts. Junction geometries are shown in Figure 3a in the main text and Figure S6. Each electrode consists of 7 layers of Au (111) with each layer having 16 Au atoms forming a 4×4 unit cell. The N atoms are attached to the Au electrode using a trimer binding motif, following a previous work.<sup>8</sup> We ensure the initial local binding geometry is similar for both the new Au–N and the dative Au←N contacts prior to relaxation. The final geometry is the geometry that minimizes the total energy. During geometry relaxation, the outer 4 layers of gold on each side move as a “rigid body” along the transport ( $z$ ) direction, with forces along  $z$ -direction calculated as an average of all  $z$ -direction forces on the layer farthest from the outmost layer. The internal distances within the “rigid body” are kept as bulk values. Coordinates of other atoms are allowed to fully relax, until forces are below 0.04 eV/Å. In this way, we achieve an optimal geometry around the molecule-gold contact, while maintaining bulk gold geometry far away from the molecule. Periodic boundary conditions and a 4×4×1 k-mesh are

used in the geometry relaxation. A 0.02 eV effective electronic temperature is used to smear the Fermi function. After the junction geometry is relaxed, transport properties are calculated using the non-equilibrium Green's function (NEGF) formalism as implemented in TranSIESTA package<sup>9</sup> with the same functional, pseudopotentials, basis sets, and k-mesh as above. 36 energy points (the default value) are used in the contour integration.

Figure S7 shows the transmissions as a function of energy relative to the Fermi level for **P2–P4** junctions formed with symmetric (two dative Au←N contacts) and asymmetric (one new Au–N and one dative Au←N contact). Figure S8 and Figure 10 shows the scattering states at Fermi level for all the seven junctions mentioned above. It is known that the standard DFT-NEGF formalism overestimates the zero-bias conductance, due to an underestimation of the Kohn-Sham level alignment between frontier orbitals of the molecule and the Fermi level of the junction<sup>10</sup>, especially when local or semi-local functionals are used. We use the DFT+ $\Sigma$  method<sup>8,10</sup>, an approximate GW self-energy correction approach, to correct the Kohn-Sham level alignment and transport properties. The correction to level alignment consists of two terms: a self-energy correction to the gas-phase HOMO-LUMO gap and a correction to the electron removal energies due to the electrostatic polarization (image-charge) of the electrodes and environment. For the gas-phase correction ( $\Sigma_{\text{gp}}$ ), we use the optimally tuned range-separated hybrid functional (OT-RSH)<sup>11</sup> to accurately calculate the HOMO energy of the gas-phase molecule. For the “image-charge” contribution ( $\Sigma_{\text{img}}$ ), we use an image plane 0.9Å from the surface, as determined previously.<sup>12</sup> The self-energy corrections for the three molecules, as well as the optimal range-separation parameter,  $\gamma$ , are listed in Table S1 below. A negative (positive) sign indicates a downward (upward) shift in the energy.

**Table S1:** Self-energy corrections and optimal range-separation parameter  $\gamma$  used in the OT-RSH functional.

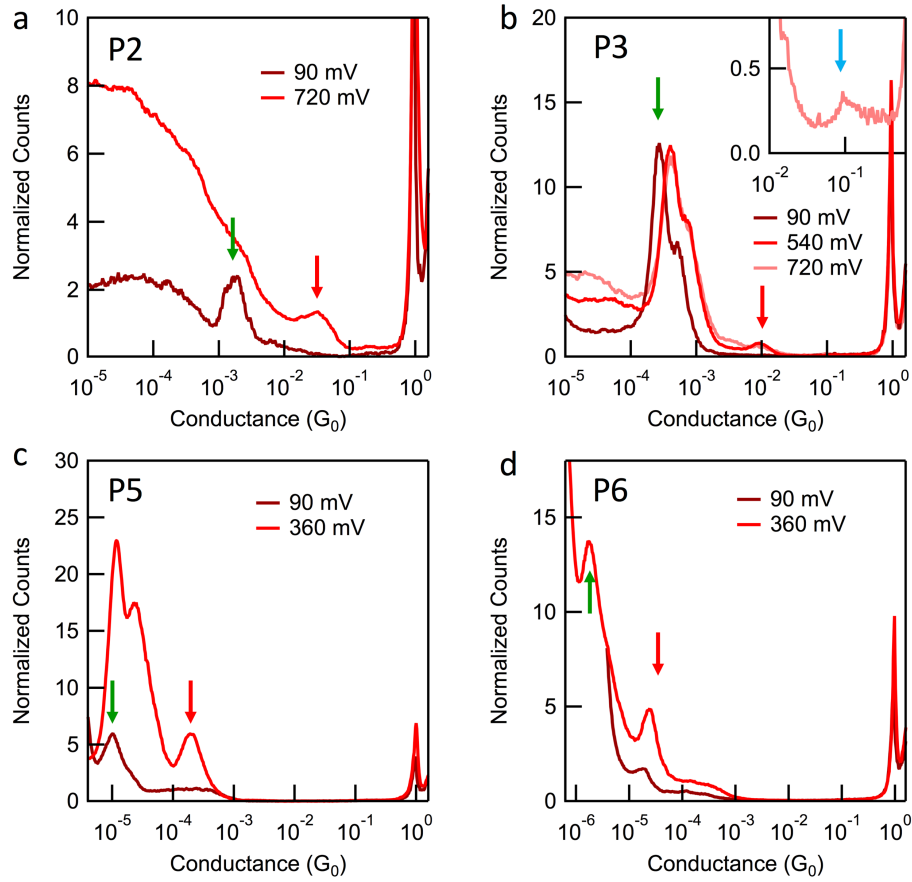
molecule	HOMO			LUMO			$\gamma$ (bohr <sup>-1</sup> )
	$\Sigma_{\text{gp}}$ (eV)	$\Sigma_{\text{img}}$ (eV)	$\Sigma_{\text{tot}}$ (eV)	$\Sigma_{\text{gp}}$ (eV)	$\Sigma_{\text{img}}$ (eV)	$\Sigma_{\text{tot}}$ (eV)	
<b>P2</b>	-2.52	0.80	-1.72	2.29	-0.74	1.55	0.19
<b>P3</b>	-2.35	0.63	-1.72	2.12	-0.57	1.55	0.17
<b>P4</b>	-2.24	0.55	-1.69	2.00	-0.48	1.52	0.16

Figure S9a compares the DFT and DFT+ $\Sigma$  transmission functions. Figure S9b compares the DFT and DFT+ $\Sigma$  conductance values together experimental measurements. One can see that with DFT+ $\Sigma$ , we achieve quantitative agreement in conductances for Low-G configurations. The DFT+ $\Sigma$  conductances calculated in this work are also in good agreement with previous results<sup>13</sup>. The DFT+ $\Sigma$   $\beta$  value is also closer to experiment than the DFT  $\beta$  as one can see in Figure S9b. The DFT+ $\Sigma$  approximation cannot be used for

High-G configurations with new Au–N contacts: once one of the H atoms is removed from one of the N atoms, the gas-phase reference becomes ill-defined. Thus, we report DFT values for these junctions in the manuscript, whose trend agrees with experiment (Figure S9b). In addition, our theoretical result agrees quantitatively in the ratios of conductances between dative Au←N contacts and the covalent Au-N contacts.

To examine the electrostatic effect of the electrolyte environment used in the experiments, we carry out transport calculations with polar HF molecules (mimicking dipole layers) on one side of the junction for **P4** molecule, as mentioned in the main text. The structures and transmission functions resulting from those calculations are shown in Figure S11.

## 5. Additional Data.



**Figure S1.** Logarithm-binned 1D histograms for (a) **P2**, (b) **P3**, (c) **P5** and (d) **P6**. The inset in (b) is a zoomed-in view of the Ultra-high-G peak at 720 mV. The Low-G, High-G and Ultra-high-G peaks are indicated by green, red and blue arrows respectively.

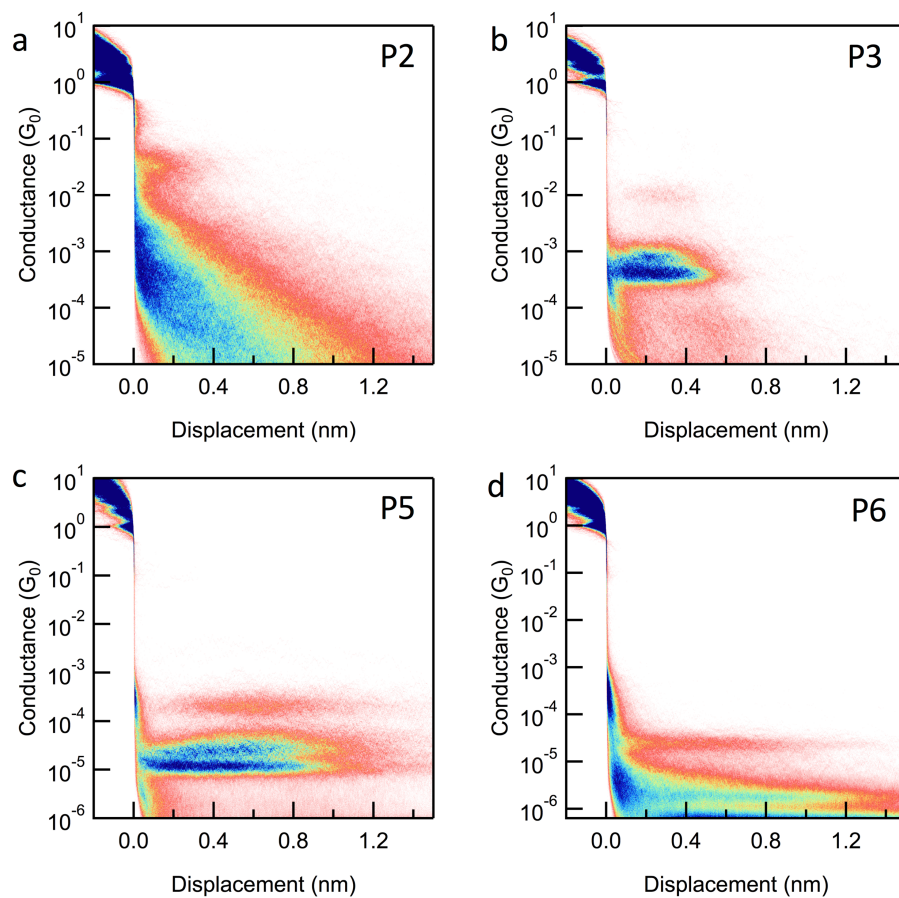


**Figure S2.** 2D conductance-displacement histograms for (a) **P2** taken at tip bias of 720 mV, (b) **P3** taken at tip bias of 540 mV, (c) **P5** and (d) **P6** taken at tip bias of 360 mV.

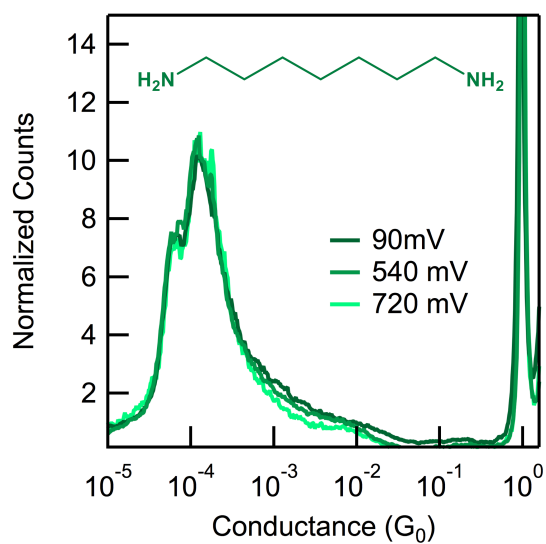


**Figure S3.** Logarithm-binned 1D histograms for 1,7-diaminoheptane.

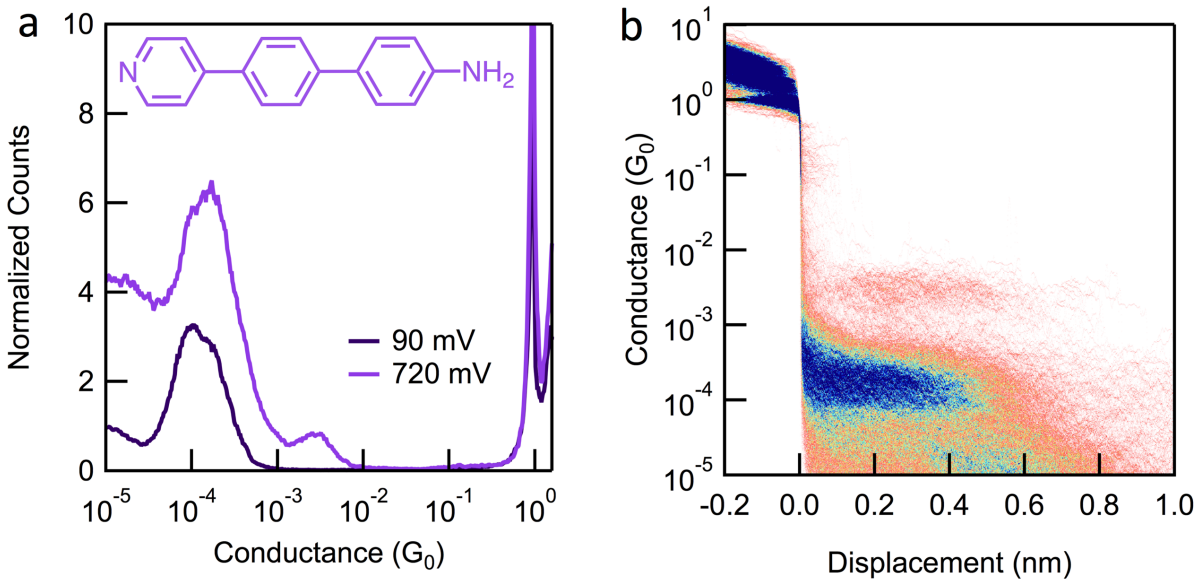


**Figure S4.** (a) Logarithm-binned 1D histograms for **P2Py**. (b) 2D conductance-displacement histogram for **P2Py** taken at tip bias of 720 mV.

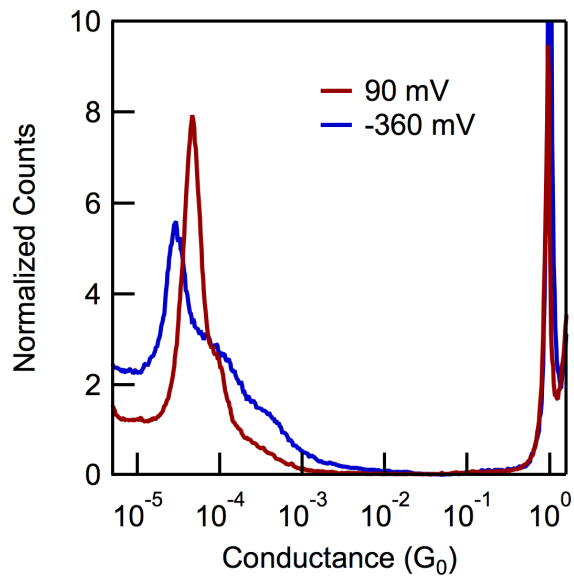


**Figure S5.** Logarithm-binned 1D histograms for **P4** at a negative bias compared with positive bias.

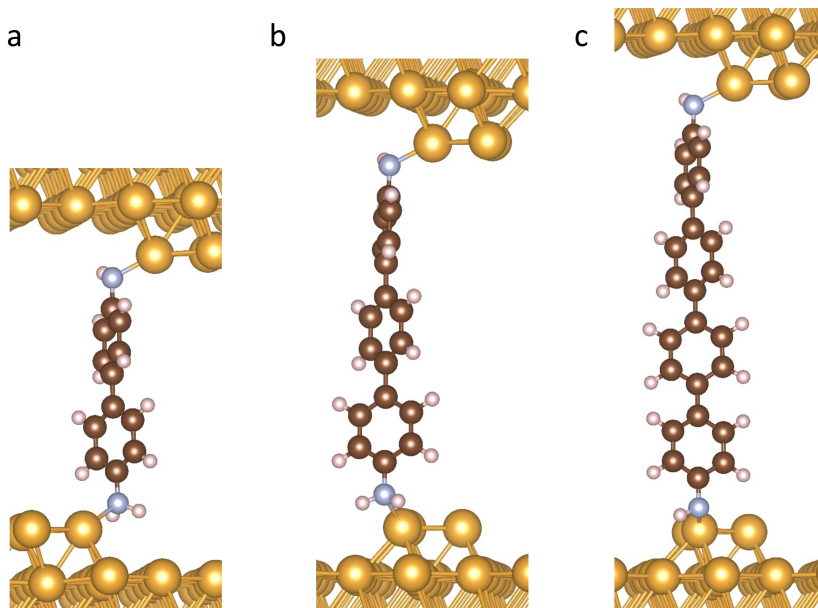


**Figure S6.** (a) Junction structure used to compute the transmission function for the (a) High-G **P2**, (b) High-G **P3** and (c) Ultra-high-G **P4** junction.

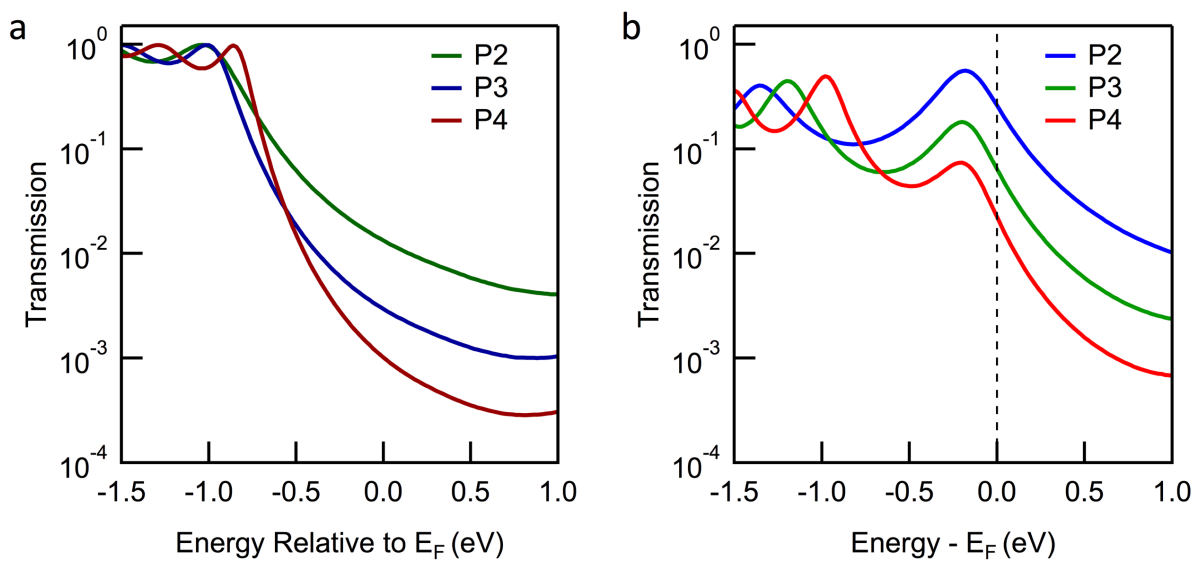


**Figure S7.** Transmission functions for (a) Low-G and (b) High-G **P2–P4** junctions.

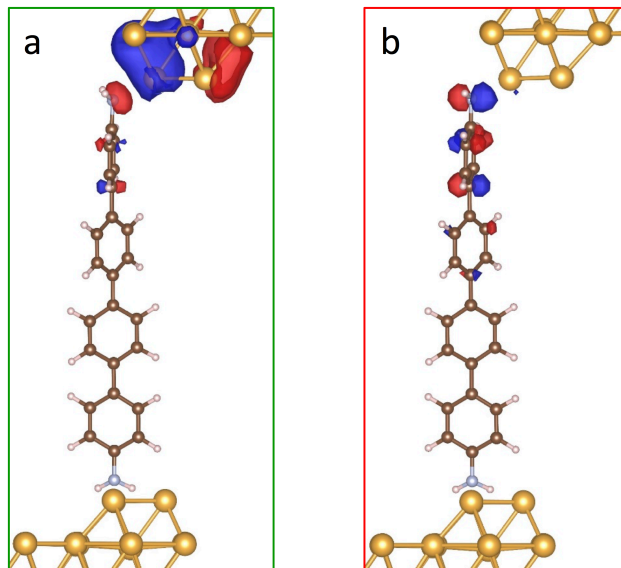


**Figure S8.** Calculated scattering state at the Fermi energy for (c) Low-G and (d) High-G **P4** junctions.

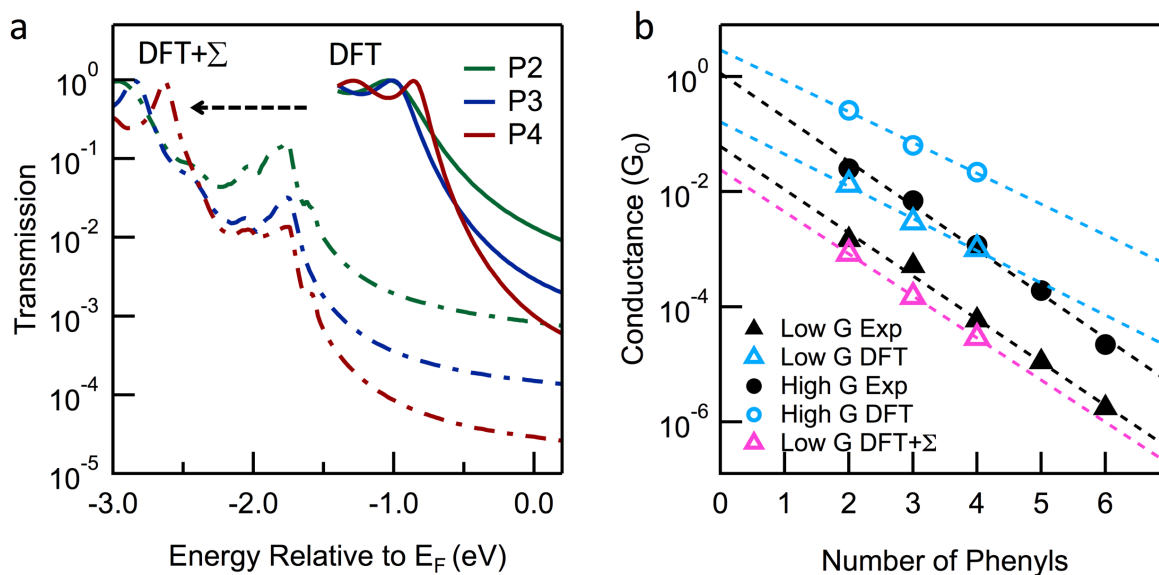


**Figure S9.** (a) Transmission functions for Low-G **P2–P4** junctions using standard DFT methods (solid) and with DFT+ $\Sigma$  (dash). (b) Conductance determined from experimental data (black) and DFT calculations (blue) plotted on a semi-log scale as a function of the number of phenyl units in the backbone for the Low-G and High-G junctions. The pink data shows the conductance determined from DFT+ $\Sigma$  calculations for the Low-G junctions.

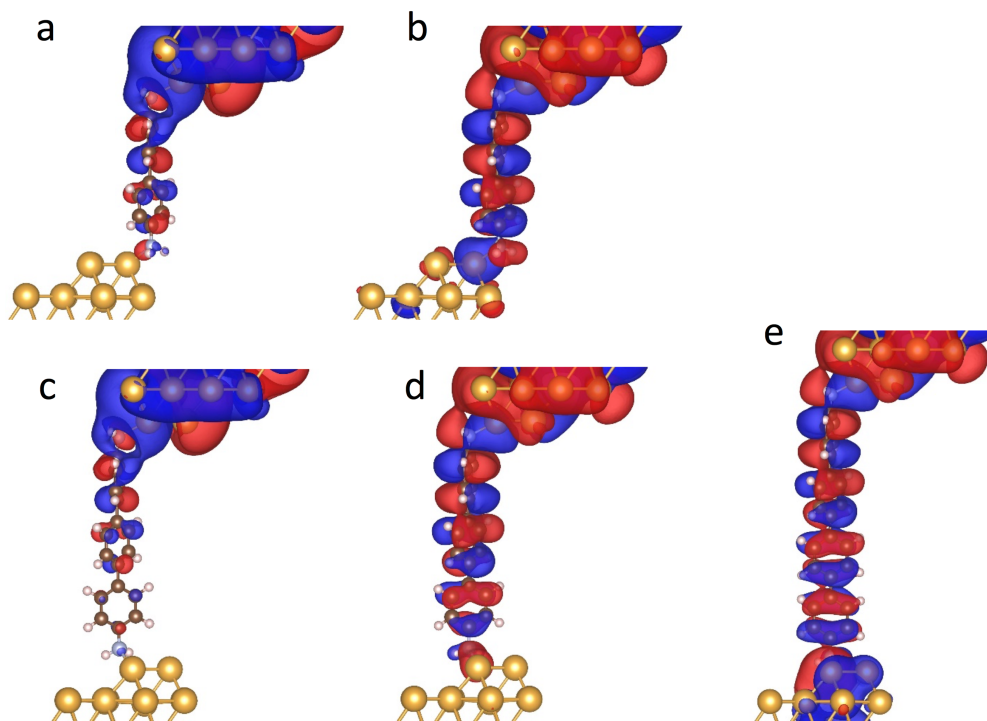


**Figure S10.** Calculated scattering state at the Fermi energy for (a, b) **P2**, (c, d) **P3** and (e) **P4**. (a, c) Low-G junctions. (b, d) High-G junctions. (e) Ultra-high-G junction.

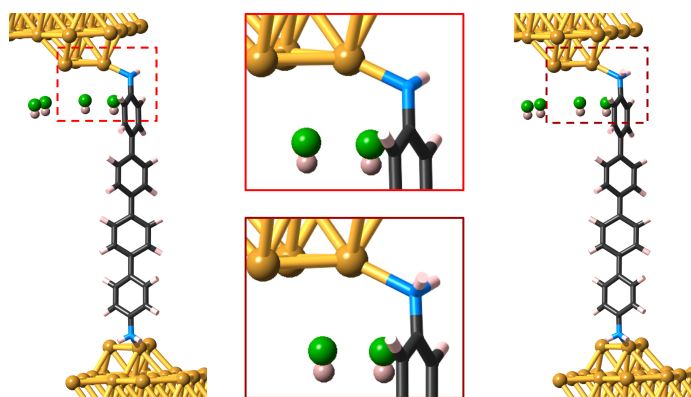


**Figure S11.** Junction structure used to compute the transmission function for Low-G (Left) and High-G (Right) **P4** junction with an HF dipole layer. The zoomed-in views in the middle show the dative Au←N and new Au–N contact.

## S5. Mass-Spectroscopy Data.

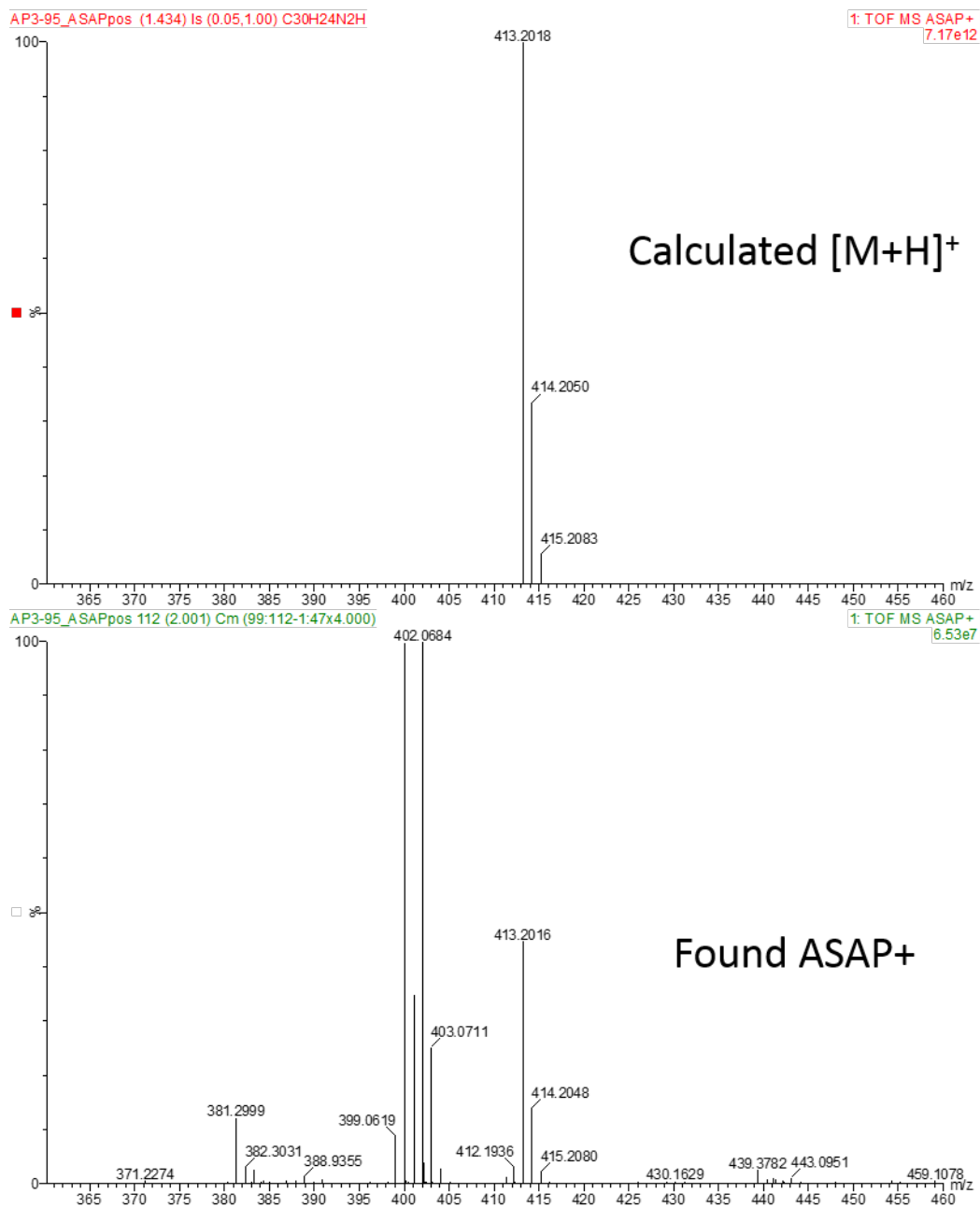
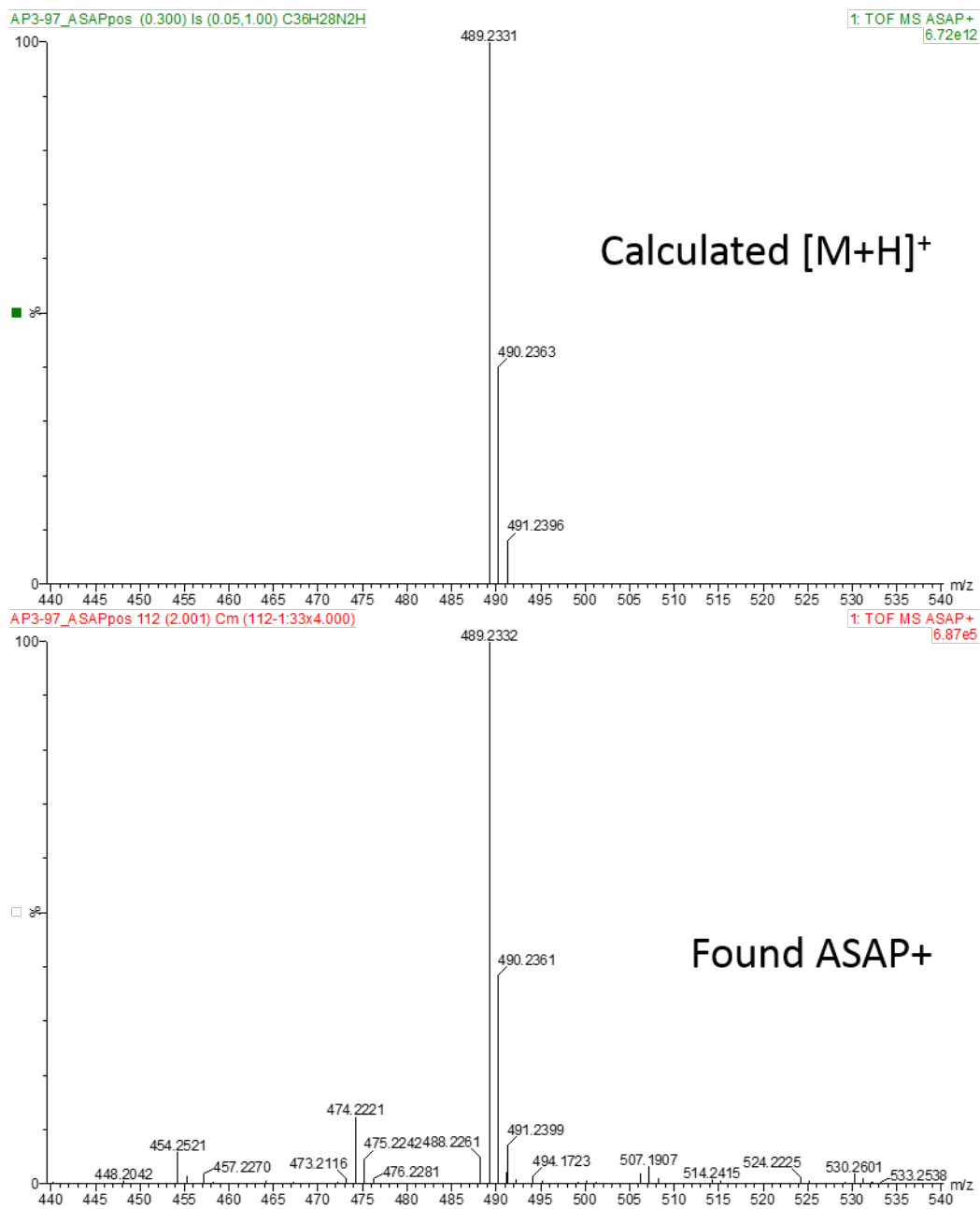
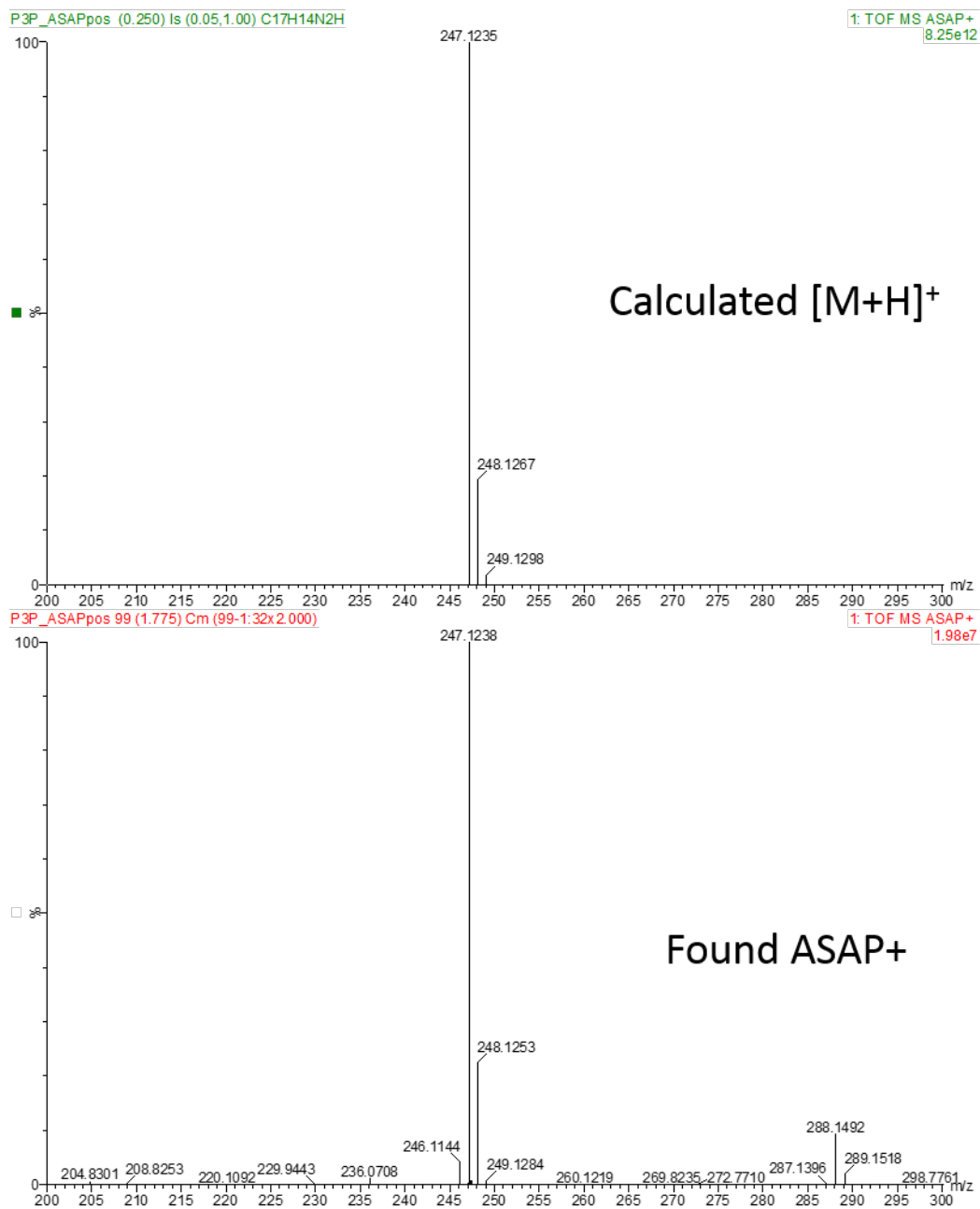


Figure S12. Calculated (top) and experimental (bottom) high-resolution mass spectrum of P5.



**Figure S13.** Calculated (top) and experimental (bottom) high-resolution mass spectrum of **P6**.



**Figure S14.** Calculated (top) and experimental (bottom) high-resolution mass spectrum of **P2Py**.

## 6. References

- 1 Schiek, M., Al-Shamery, K. & Lützen, A. *Synthesis* **2007**, *4*, 613.
- 2 Péres, L. O., Guillet, F. & Froyer, G. *Org. Biomol. Chem.* **2004**, *2*, 452.
- 3 Sánchez-Molina, M., López-Romero, J. M., Hierrezuelo-León, J., Martín-Rufián, M. Díaz, A., Valpuesta, M. & Contreras-Cáceres, R. *Asian J. Org. Chem.* **2016**, *5*, 550.
- 4 Venkataraman, L., Klare, J. E., Nuckolls, C., Hybertsen, M. S. & Steigerwald, M. L. *Nature* **2006**, *442*, 904.
- 5 Nagahara, L. A., Thundat, T. & Lindsay, S. M. *Rev. Sci. Inst.* **1989**, *60*, 3128.
- 6 Perdew, J. P., Burke, K. & Ernzerhof, M. *Phys. Rev. Lett.* **1996**, *77*, 3865.
- 7 Soler, J. M., Artacho, E., Gale, J. D., García, A., Junquera, J., Ordejón, P. & Sánchez-Portal, D. *J. Phys.:Cond. Mat.* **2002**, *14*, 2745.
- 8 Quek, S. Y., Venkataraman, L., Choi, H. J., Louie, S. G., Hybertsen, M. S. & Neaton, J. B. *Nano Lett.* **2007**, *7*, 3477.
- 9 Brandbyge, M., Mozos, J.-L., Ordejón, P., Taylor, J. & Stokbro, K. *Phys. Rev. B* **2002**, *65*, 165401.
- 10 Neaton, J. B., Hybertsen, M. S. & Louie, S. G. *Phys. Rev. Lett.* **2006**, *97*, 216405.
- 11 Refaely-Abramson, S., Sharifzadeh, S., Govind, N., Autschbach, J., Neaton, J. B., Baer, R. & Kronik, L. *Phys. Rev. Lett.* **2012**, *109*, 226405.
- 12 Egger, D. A., Liu, Z. F., Neaton, J. B. & Kronik, L. *Nano Lett.* **2015**, *15*, 2448.
- 13 Quek, S. Y. Q. S. Y., Choi, H. J., Louie, S. G. & Neaton, J. B. *ACS Nano* **2011**, *5*, 551.